Volume 6 | Number 11 | November 2014 | Pages 1001–1102

Integrative Biology

Interdisciplinary approaches for molecular and cellular life sciences

www.rsc.org/ibiology

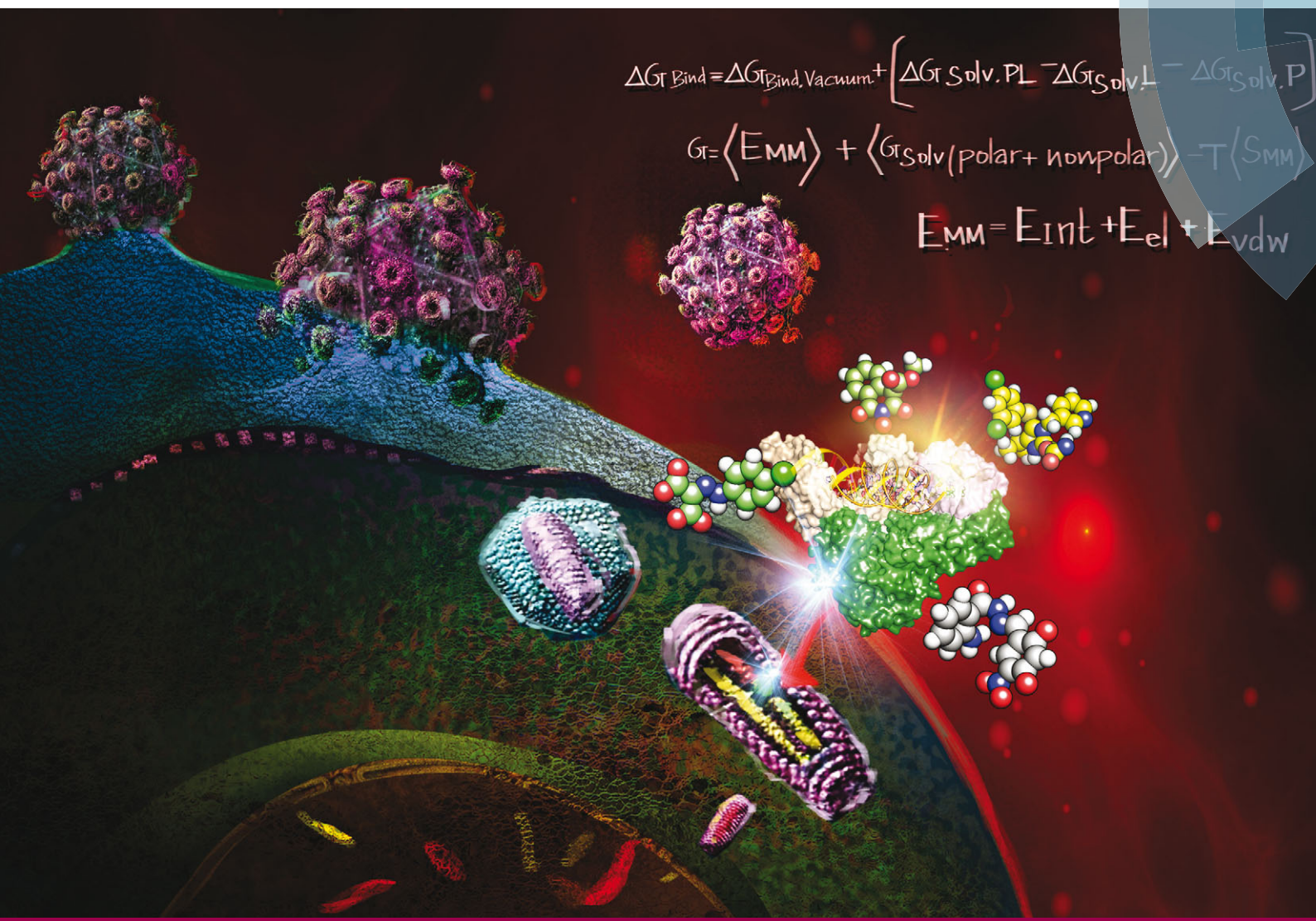

Themed issue: Computational Integrative Biology

ISSN 1757-9694

ROYAL SOCIETY OF CHEMISTRY

PAPER
Vasanthanathan Poongavanam *et al.*
Binding free energy based structural dynamics analysis of HIV-1 RT RNase H–inhibitor complexes

Indexed in Medline!

Integrative Biology

PAPER

View Article Online
View Journal | View Issue

Cite this: *Integr. Biol.*, 2014, 6, 1010

Binding free energy based structural dynamics analysis of HIV-1 RT RNase H–inhibitor complexes†

Vasanthanathan Poongavanam,* Jógvan Magnus Haugaard Olsen and Jacob Kongsted

Received 21st May 2014,
Accepted 5th August 2014

DOI: 10.1039/c4ib00111g

www.rsc.org/ibiology

Accurate prediction of binding free energies associated with small molecules binding to a receptor is a major challenge in drug design processes. To achieve this goal many computational methods have been developed ranging from highly efficient empirical based docking schemes to high accuracy methods based on *e.g.* free energy calculations. In this study, binding affinity predictions for a set of HIV-1 RNase H inhibitors have been performed using MM-PB(GB)/SA methods. The current study describes in detail how the choice of initial ligand structures, *e.g.* protonation states, impacts the predicted ranking of the compounds. In addition we study the structural dynamics of the RNase H complexes using molecular dynamics. The role of each residue contribution to the overall binding free energy is also explored and used to explain the variations in the inhibition potency. The results reported here can be useful for design of small molecules against RNase H activity in the development of effective drugs for HIV treatment.

Insight, innovation, integration

To unveil structural dynamical aspects of HIV-1 RT RNase H (RNH) we have examined the importance of ligand protonation states in order to achieve accurate prediction of binding affinities using the MM-PB(GB)/SA methods. From the free energy calculation and structural dynamics investigations, we find that the protonation states of the ligands greatly impact the protein–ligand binding process. In addition, we observe that the inter-magnesium ion distances as well as the magnesium ion–residue and magnesium ion–ligand interactions are strongly dependent on both the protonation states and the number of oxygen atoms in the ligands. Altogether these factors strongly influence chelation formation, which impacts the overall ligand affinity. Furthermore, the interaction energy contributions due to Glu478 and Thr497 are found to be highly correlated with the binding affinity. The findings of this study are important for further RNH inhibitor design for better therapeutics.

1. Introduction

Human immunodeficiency virus type 1 (HIV-1) reverse transcriptase associated ribonuclease H (RNase H or RNH) is an attractive chemo-target for development of anti-HIV agents.[1,2] It is one of the two essential domains of HIV-1 reverse transcriptase (RT, p66 subunit), which plays a key role in viral replication. During the viral replication process, the genomic single stranded RNA (viral) is transformed into a RNA:DNA hybrid duplex by the polymerase domain with the help of a cellular RNA primer (specifically tRNAlys3). Subsequently, the RNH domain removes the RNA strand from the hybrid and facilitates the first strand transfer which leads to formation of purine rich sequences of HIV RNA (also called ''polypurine tract'' (PPT)). Here, PPT serves as a primer for the synthesis of viral (+) DNA strands and subsequently RNase H removes the PPT portion after priming of (+) DNA synthesis. The RNase H catalytic site consists of a conserved DDDE motif (Asp443, Asp498, Asp549 and Glu478), which is coordinated with two catalytically active magnesium ions (Mg^{2+}). In the catalytic process, the magnesium ions initiate the formation of a nucleophile (OH^-) (from the active site water molecules), which attacks the RNH substrate (RNA:DNA hybrid) in order to execute the digestion process.[3,4]

The majority of the currently marketed antiviral drugs that have been approved by the FDA for the treatment of HIV infections are RT inhibitors that particularly inhibit at the polymerase domain.[5,6] However, there is a large number of RNH inhibitors reported and some of these have entered into clinical trial,[7,8] but none of these inhibitors have yet reached the market. The catalytic role of RNH can be diminished

Department of Physics, Chemistry and Pharmacy, University of Southern Denmark, Campusvej 55, DK-5230 Odense M, Denmark. E-mail: nathan@sdu.dk

† Electronic supplementary information (ESI) available. See DOI: 10.1039/c4ib00111g

through two inhibitory mechanisms: (1) compounds that block the magnesium ions availability to the catalytic process (also called active site binders) and (2) compounds that bind at the allosteric site (located near to the p51 thumb) and change the conformation of RNH which disables the substrate binding (RNA:DNA hybrid) at the catalytic site. Compounds such as NSC727447 (a vinylogous urea) and acylhydrazones bind at the allosteric site.[9–11] Compared to the inhibition of RNH through active site binding, an allosteric inhibition provides an attractive drug target for HIV-1 RNH inhibition since compounds that bind at this site will not interfere with human RNase H1[12] due to different locations of the RNH allosteric site in humans and virus. However, only a small number of allosteric inhibition compounds have been reported. On the other hand, a large number of active site binders have been reported and some even entered into the clinical phase.[7] The reason for such a large number of studies in this class is due to a well defined "pharmacophore" pattern among these compounds, *e.g.* pyrimidinone, diketo, tropolone, *N*-hydroxyimide, diones *etc.*[8] Another possible reason is that many of these compounds also exhibit HIV-1 integrase activity (so-called dual inhibition).[13] Dual inhibition also represents a way to achieve HAART (highly active antiretroviral therapy).[14]

The topology of the HIV-1 RNH active site is well characterized as being small, slightly hydrophobic and containing a highly electrostatic negative potential surface, which is primarily formed by the DDDE motif coordinated with two catalytically active magnesium ions (Fig. 1).[4,12,15–17] Very recently, molecular modeling methods have been used to study and predict RNase H inhibition using virtual screening models for the active site[18,19] and the allosteric site.[11,20] However, there exists only a very limited number of studies that explore the structural dynamics of the RNH domain.[21] Investigation of the structural dynamics of RNH will provide highly valuable information for inhibitor design, *e.g.*, mode of ligand recognition by the protein, structural changes upon ligand binding, all factors that influence the ligand binding affinity. In a previous study we have developed efficient virtual screening models[18] (*e.g.* structure and ligand based). Such models are very useful when identifying inhibitors from non-inhibitors based on compounds extracted from large databases, however, none of the previously developed models are suitable to accurately rank the binders according to their binding affinity. The aim of the present study is to rank a set of known RNH inhibitors according to their activities using the MM-PB(GB)/SA method and to use these binding affinities as initial structural validations to further study and analyze the dynamics of RNH–inhibitor complexes. Therefore, this work is divided into two parts. The first part discusses how the protonation states of the ligands influence the binding affinity ranking through MM-PB(GB)/SA calculations and the second part investigates the structural dynamics of RNase H–inhibitor complexes. Especially we investigate in detail the magnesium ions, bound water and residue dynamics and interactions with the inhibitors.

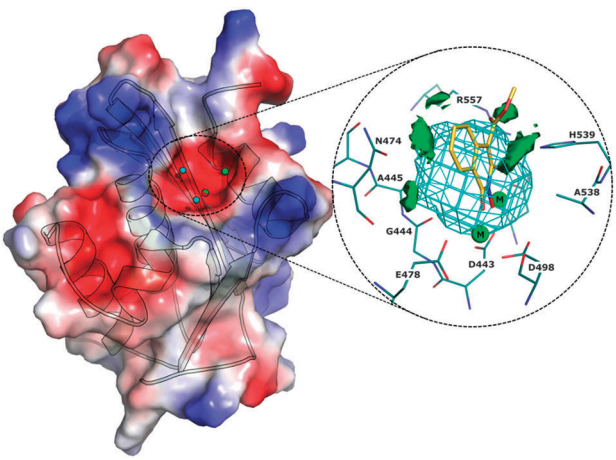

Fig. 1 Electrostatic potential surface of the HIV-RT associated RNase H domain model. The active site of RNH characterized with molecular interaction fields is shown in the circle including the cavity (cyan mesh), hydrophobic regions (green surface), inhibitors (yellow) and magnesium ions (green sphere).

2. Computational methods and materials

2.1. Preparation of protein–ligand complexes

The computational model of the HIV-1 RT associated RNase H domain was constructed from an X-ray crystal structure (resolution of 1.4 Å) from the Protein Data Bank (PDB ID: 3QIO).[15] In the deposited crystal structure of the RNase H domain with *N*-hydroxy quinazolinediones (bound active site inhibitor), 12 residues were missing and the structure was determined with manganese (Mn^{2+}) ions instead of the two catalytically active magnesium ions (Mg^{2+}). Therefore, the structure of the RNase H domain was reconstructed by adding the missing residues using the Swiss-Model.[22] The obtained protein model was then imported into the Maestro module available in the Schrödinger suite[23] and the structure was further optimized using the Protein Preparation Wizard.[24] This optimization includes adding hydrogen atoms, assigning bond orders and building di-sulfide bonds and replacing the Mn^{2+} ions with Mg^{2+} ions. The protonation states of all of the ionizable residues were predicted by PROPKA[25] provided in the Protein Preparation Wizard in the presence of the Mg^{2+} ions at the active site. An optimized structure model was finally found by energy minimization (only hydrogen atoms) using the OPLS2005 force field.

A set of six chemically diverse RNase H inhibitors with known activity (IC_{50}) was collected from the literature (Fig. 2). All compounds belong to active site direct inhibitors, except BHMP07 which is an allosteric RNH inhibitor. Due to the long side chain of BHMP07 this molecule interacts with residues that also interact with the active site binders (Fig. S1, ESI†). The binding pose of BHMP07 used in this study is very similar to a previously predicted binding pose[26] and is characterized by interactions with residues such as Asn474 (H-bonding), Gln500 (H-bonding), Tyr501 (π–π stacking), Asp498 (H-bonding), Gly444 (H-bonding) and Asp443 (H-bonding). The 3D structure of all

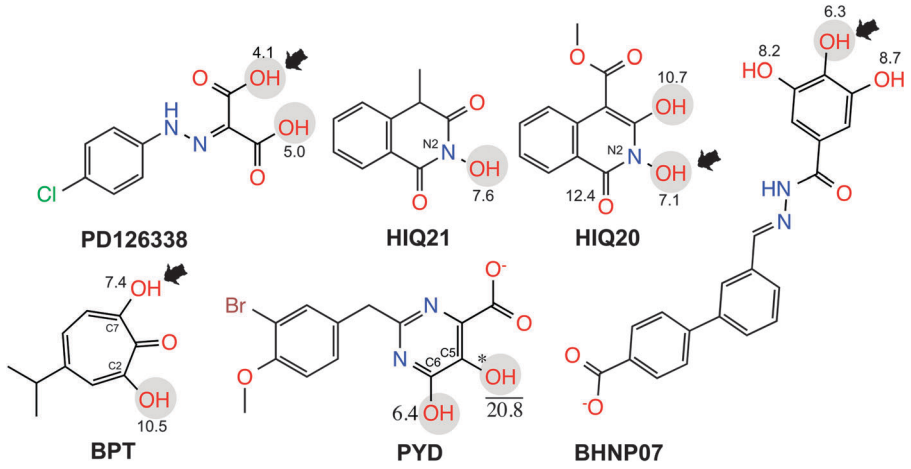

Fig. 2 2D structure of RNase H inhibitors used in the present investigation. Ionization states used for the free energy calculations are highlighted. The pK_a prediction for the enolic sites is shown (see text for details). Deprotonation states used in scenario ONE and scenario TWO are shown in gray circles and black arrow, respectively. The position indicated with * could not be determined due to convergence issues.

molecules was built in the Maestro module and pre-processed using the LigPrep tool in the Schrödinger suite. The pK_a for each ionizable group in the molecules was predicted using either Epik (an empirical based tool)[27] or quantum mechanics (QM) based pK_a prediction tools implemented in the Jaguar program[28] (see Results section for more detail).

Glide[29] (a grid-based exhaustive search algorithm), from the Schrödinger suite, was used to obtain initial conformations of the ligands in the active site of RNase H. Before the ligands were docked into the RNase H binding site, the active site is defined by the receptor grid generation procedure implemented in the Glide module. The bound ligand (3-hydroxy 6-(phenylsulfonyl)-quinazoline-2,4-(1*H*,3*H*)-dione) was set as the centroid of the grid box and water molecules <3 Å from the bound ligand in the active site were kept for the docking experiments. The Glidescore (Standard Precision mode) was used to rank the docking poses.

2.2. Molecular dynamics simulation setup

All molecular dynamics simulations were performed and analyzed using the Amber 12 software.[30] Before the system setup for MD, all six ligands shown in Fig. 2 were geometry optimized with HF/6-31G** using Gaussian 09[31] and the atomic charges used for the molecular dynamics were calculated from the ESP (electrostatic potential) using B3LYP-IEFPCM/cc-pVTZ. These atomic charges were fitted using the RESP procedure as implemented in the Antechamber module of the Amber 12 software. The *tleap* tool in the Amber suite was used to build coordinate and parameter (Amber ff03 force field) input files. Subsequently, TIP3P water (solvent) molecules were added with a 10 Å buffering distance between the edges of the truncated octahedron box. In order to avoid edge effects, periodic boundary conditions were applied during the molecular dynamics simulations. Energy minimization was carried out in two steps: first, the system was minimized using a steepest descent minimization with all heavy atoms restrained. The maximum number of minimization cycles was set to 1000. In the second stage of the minimization, the entire system was energy minimized and no positional restraints were applied at this stage.

In the process of thermalization, initial velocities were generated from a Maxwell–Boltzmann distribution at 100 K and gradually increased to 300 K at constant volume over a 200 ps MD simulation. After the thermalization process, the system was equilibrated at constant temperature (300 K) and pressure (1 bar) using the Berendsen coupling algorithm[32] for another 500 ps MD simulation. After the equilibration step, the MD production run was started for 20 ns (10 000 000 MD steps with 0.002 time steps). The SHAKE algorithm was used to constrain the lengths of all bonds involving hydrogen atoms. Coordinates were saved every 10 ps from the 20 ns simulation for the analysis; in total 2000 snapshots were used for binding free energy calculations and investigations.

2.3. MM-PB(GB)/SA based affinity prediction

MM-PB(GB)/SA is a force-field based method which employs molecular mechanics, the Generalized Born (GB)/Poisson Boltzmann (PB) solvation models and a solvent accessibility method to approximate the free energies of binding based on snapshots extracted from MD simulations.[33–35] The binding free energy (ΔG_{Bind}) of the protein–ligand complex is calculated based on eqn (1)

$$\Delta G_{\text{Bind}} = \Delta G_{\text{Bind,Vacuum}} + (\Delta G_{\text{Solv,PL}} - \Delta G_{\text{Solv,L}} - \Delta G_{\text{Solv,P}}) \quad (1)$$

where ΔG_{Bind} and $\Delta G_{\text{Bind,Vacuum}}$ correspond to the free energy difference between the bound and unbound states of a complex in solvent and vacuum, respectively. ΔG_{Solv} ($\Delta G_{\text{Solv,L}}$, $\Delta G_{\text{Solv,P}}$ and $\Delta G_{\text{Solv,PL}}$) represent the change in free energy between the solvated and vacuum states of a ligand, receptor or complex. These different components can be calculated as a sum of three terms:

$$G = \langle E_{\text{MM}} \rangle + \langle G_{\text{Solv(polar+nonpolar)}} \rangle - T\langle S_{\text{MM}} \rangle \quad (2)$$

$$E_{\text{MM}} = E_{\text{Int}} + E_{\text{el}} + E_{\text{vdW}} \quad (3)$$

where E_{MM} is MM energy of the molecules. E_{MM} is the sum of the internal energy (E_{Int}) of the molecule(s) (*i.e.* bonded terms)

and E_{el} and E_{vdW}, which represent the intermolecular electrostatic and van der Waals interactions, respectively. In order to reduce the computational time, and to obtain stable energies, a single-trajectory is normally used for the ligand, protein and complex, *i.e.* only the protein–ligand complex is explicitly simulated by MD.[35] Thereby the E_{Int} term cancels in the calculation of ΔG_{Bind}. G_{Solv} is the sum of the polar and non-polar solvation energies of the molecules, estimated either from the GB or PB approximations and combined with a solvent accessible surface area (SASA) method for the non-polar part of the solvation energy. T is the temperature and S_{MM} is the entropy which is estimated from a normal-mode analysis calculated at the molecular mechanical level.

The binding free energies (ΔG_{Bind}) for all protein–ligand complexes were calculated according to eqn (2) and (3) using the MMPBSA.py script in Amber 12 based on the use of 2000 snapshots extracted from the 20 ns MD simulation. The implementation of MMPBSA.py in Amber 12 is well described in the original publication.[36] All MM-PB(GB)/SA calculations are based on the ''single-trajectory MD simulation'', meaning that no separate MD simulations were run for the free ligands, however, for the structural investigation, an MD simulation for the receptor (the so-called Apo form) was additionally performed.

3. Results and discussion

3.1. Part 1: optimization of binding free energy models

The obtained free energies of binding from various stages of refinement of the ligands are here discussed together with the ligand preparation steps. Initially, in order to get a good correlation between observed and calculated activities, the reported biological activity (IC_{50}) data were converted into pIC_{50} values. For clarity, the obtained results are discussed in three scenarios as follows.

3.1.1. Scenario ONE: can we trust the default settings? After the 3D molecular structures of the ligands were built in the Maestro module of the Schrödinger suite,[23] and all ligands were preprocessed using the LigPrep module of the Schrödinger suite, this preprocess includes the prediction of protonation states for each ligands at pH 7.0 ± 2.0 using the Epik tool[27] and energy minimization using the OPLS2005 force field. This procedure is quite commonly followed by the computational chemist, because it represents an efficient way of handling a large number of compounds. Protonation states of all ligands used for the MD simulation are shown in Fig. 2. Each ligand was docked into the RNase H model using the Glide program[29] and the resulting protein–ligand complexes were then used for MD simulations as described in the Computational method section.

3.1.2. Scenario ONE: results. From the MD simulations of each complex, 2000 snapshots were analyzed with respect to energy convergence in order to make sure that the protein–ligand complex is energetically stable (Fig. S2, ESI†). To further evaluate the difference in the binding free-energy for each complex, the MM-PB(GA)/SA methods were used to calculate binding energies for 2000 snapshots from the 20 ns simulation. The summary of the free energies obtained for each complex is provided in Table 1 which shows all the energy terms of eqn (2) and (3) together with experimentally measured activities as well as the total predicted binding free energies. Upon correlating

Table 1 Summary of energies obtained from MM-PB(GB)/SA methods using various scenarios

		MM-GBSA						MM-PBSA					
	Compound	PYD	BPT	BHNP07	PD	HIQ20	HIQ21	PYD	BPT	BHNP07	PD	HIQ20	HIQ21
Scenario ONE	IC_{50} (μM)	0.9	0.21	0.20	6.1	0.061	38.8	0.9	0.21	0.20	6.1	0.061	38.8
	pIC_{50} (μM)	6.05	6.68	6.70	5.21	7.21	4.41	6.05	6.68	6.70	5.21	7.21	4.41
	E_{vdW}	0.64	−3.31	−6.15	4.21	1.90	−4.42	0.64	−3.31	−6.15	4.21	1.90	−4.42
	E_{Ele}	−531.76	−302.46	−303.09	−530.90	−615.87	−360.99	−531.76	−302.46	−303.09	−530.90	−615.87	−360.99
	ΔG_{Solv}	459.52	268.45	277.76	443.27	512.84	301.44	474.61	278.11	300.95	450.96	520.66	308.23
	ΔG_{gas}	−531.11	−305.78	−309.23	−526.69	−613.97	−365.41	−531.11	−305.77	−309.24	−526.69	−613.97	−365.41
	ΔG	−71.60	−37.32	−31.48	−83.42	−101.13	−63.97	−56.51	−27.66	−8.28	−75.73	−93.31	−57.18
	$T^*\Delta S$	−27.07	−19.09	−22.22	−27.25	−28.78	−24.05	−27.07	−19.09	−22.22	−27.25	−28.78	−24.05
Scenario TWO	E_{vdW}	−0.29	−1.57	—	−5.41	−7.36	−12.10	−0.29	−1.57	—	−5.41	−7.36	−12.10
	E_{Ele}	−21.91	−295.80	—	−248.79	−315.49	−44.85	−21.91	−295.80	—	−248.79	−315.49	−44.85
	ΔG_{gas}	−22.19	−297.37	—	−254.20	−322.84	−56.95	−22.19	−297.37	—	−254.20	−322.84	−56.95
	ΔG_{Solv}	22.18	259.47	—	207.43	274.38	53.54	23.24	274.29	—	233.19	286.12	64.05
	ΔG	−0.02	−37.90	—	−46.77	−48.46	−3.41	1.05	−23.08	—	−21.00	−36.73	7.10
	$T^*\Delta S$	−11.35	−18.98		−21.86	−23.82	−17.77						
Scenario THREE	E_{vdW}	−5.42	—	—	−5.70	—	—	−5.42	—	—	−5.70	—	—
	E_{Ele}	−271.62	—	—	−249.79	—	—	−271.62	—	—	−249.79	—	—
	ΔG_{gas}	−277.04	—	—	−255.49	—	—	−277.04	—	—	−255.49	—	—
	ΔG_{Solv}	234.61	—	—	244.74	—	—	247.59	—	—	244.50	—	—
	ΔG	−42.43	—	—	−10.75	—	—	−29.45	—	—	−10.98	—	—
	$T^*\Delta S$	[a]			−21.98								

Note: all energy components are extracted from the differences (average) of $\Delta G_{Complex} - \Delta G_{Receptor} - \Delta G_{Ligand}$. The results refer to averages over 2000 frames and all units are reported in kcal mol^{-1}. Abbreviation: E_{vdW} = van der Waals energy, E_{ele} = electrostatic energy, ΔG_{gas} = sum of van der Waals energy + electrostatic energy + internal energy, ΔG_{Solv} = solvation energy (polar and non-polar), ΔS = entropy, T = 298.15 K. [a] Could not be calculated due to energy convergence issues.

calculated binding affinities against the experimental values we excluded the Entropy term. This is due to the fact that in some cases the Entropic term could not be calculated due to convergence issues. As clearly seen from Table 1, in both the MM-PB/SA and MM-GB/SA methods, the van der Waals term for PYD, PD and HIQ20 is unfavorable and contributes least to the binding energy, whereas the electrostatic term is favorable and dominates the overall binding affinity for all the compounds. Comparison of the calculated binding affinities with experiment reveals that for the majority of the compounds large deviations are found by both methods. However, HIQ20, the highly active compound (IC_{50} = 0.061 μM) in the dataset, is correctly predicted as a highly active compound by both the MM-PB/SA and MM-GB/SA methods (−93.31/−101.13 kcal mol^{-1}). Moreover, the compounds that possess sub-micro molar inhibition (*e.g.*, BPT/BHNP07, IC_{50} = 0.2 μM) are poorly predicted (−37.48/−31.48 kcal mol^{-1} from MM-GB/SA and −27.66/−8.28 kcal mol^{-1} from MM-PB/SA) compared to the compound that possesses poor inhibition (HIQ21, IC_{50} = 38 μM) with difference of ∼−30 kcal mol^{-1} found by both methods.

Similar predictions were observed for compounds PD and PYD, which show moderate inhibition, but according to the predicted binding energies, both compounds are found as highly active compounds. This overestimation might be due to the presence of carboxylic acid and hydroxyl groups in these molecules, which bind strongly with the magnesium ions in the RNase H catalytic site. However, this was not reflected in the experimental activity (*i.e.* IC_{50}). This observation raises the question whether the correct protonation states for the ligands have been used in the docking and MD simulations. As shown in Fig. 3A, the overall result of this potentially incorrect ionization greatly influences the ranking by having a poor correlation (R^2 = 0.006 for MMGBSA and R^2 = 0.0221 for MMPBSA) between the binding free energies and experimental activities.

3.1.3. Scenario TWO: do QM-based methods predict the correct ionization state? As seen in scenario ONE the ionization states of the ligands may have a significant influence on the binding free energy difference between the compounds since chelation is the main driving force for the binding.[7] Thus, the pK_a value for each ionizable group in the molecules was calculated using the quantum mechanics (QM) based pK_a method implemented in the Jaguar program.[28]

3.1.4. Scenario TWO: results. The pK_a value for each ionizable site is shown in Fig. 2. As seen from Fig. 2, except for compound BHNP07, the compounds have very different ionization states as compared to the ionization states used in scenario ONE. For instance, the hydroxyl group at the C7 position of BPT now has a favorable pK_a (7.4) for ionization at biological pH compared to the hydroxyl group at C2 (pK_a = 10.5). The hydroxyl group at the N2 position of compound HIQ21 has a pK_a of 7.6. Although the pK_a value is close to the biological pH, we assume that a portion of the compound is still in the unionized form at pH 7.4. Thus, we kept this molecule as unionized.

The hydroxyl group at the N2 position of compound HIQ20 has a favorable pK_a for deprotonation. Compound PYD has a carboxylic acid and two hydroxyl groups at the C5 and C6 positions. The pK_a of the hydroxyl group at the C6 position is

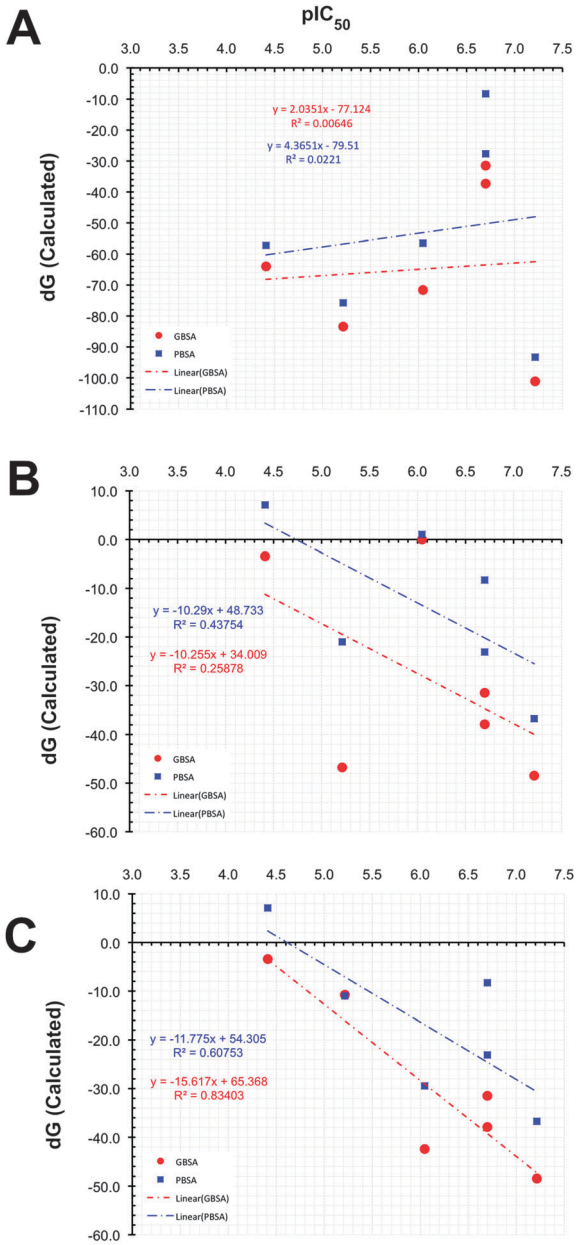

Fig. 3 Correlation between the observed activity and the MM-PB(GB)/SA predicted activity according to scenario ONE (A), scenario TWO (B), and scenario THREE (C).

6.4 and the pK_a for the hydroxyl group at the C5 position could not be calculated due to the convergence issues.

In addition, when both the carboxylic acid and hydroxyl group at C6 are deprotonated, the pK_a of the hydroxyl group at C5 is 20.8. Due to the proton on the (C6) OH group far from the COOH group, OH (C6) will not deprotonate due to the fact the OH (C5) next to it is partially negatively charged due to the share of a proton with the neighboring COO– group. If OH (C6) would deprotonate, there might be an unfavorable charge–charge interaction within these groups. Therefore, only the carboxylic acid is kept in the deprotonated form, whereas the two hydroxyl groups remain protonated in scenario TWO. The compound PD has two

terminal carboxylic acid groups, which has unequal electron distribution due to the neighboring hydrazine group. Thus, the group (COOH) close to the NH atoms is easily deprotonated (pK_a = 4.1). In the binding affinity calculation we kept one COOH group in the deprotonated form and the other COOH remains protonated in order to avoid unfavorable charge–charge interaction between the two acid groups.

In scenario TWO, the same ionization state was used for BHNP07 as in scenario ONE. Once again the newly predicted ionized forms were built, energy minimized, docked and the MD simulations were carried out for 20 ns as described in the Computational method section.

From Table 1, it can now be noticed for scenario TWO that there is a remarkable change in the predicted binding free energies of PD, PYD and HIQ21 as found by the MM-PB(GA)/SA methods. As seen from Fig. 3B the correlation coefficient (R^2) between the predicted and observed activities is significantly improved from 0.006 to 0.25 for MM-GB/SA and 0.02 to 0.44 for MM-PB/SA. No significant change was observed in the binding free energy of BPT based on the MM-GB/SA method, however, it should be noted that a reduction of nearly −5 kcal mol^{-1} is predicted by the MM-PB/SA method in scenario TWO compared to scenario ONE. The compound HIQ21 is now predicted as a poor binder by both methods compared to scenario ONE. This is a remarkable improvement. The compound PD is still being predicted as a strong binder by the MM-PB(GB)/SA methods with a binding affinity of −21.00/−46.77 kcal mol^{-1}, respectively. Compared to compound HIQ20, which is a strong binder (−38.73/−48.46 kcal mol^{-1}), the binding energy of PD is nearly in the same range. On the other hand, the compound PYD is predicted as a poor binder with a binding energy of −0.018 and 1.045 kcal mol^{-1} from MM-GB/SA and MM-PB/SA, respectively. This reflects that indeed the ionization state plays an essential role for binding affinity prediction. Overall, in scenario TWO the binding energies and ranking have significantly improved, however, the compounds PYD and PD are still outliers. This observation led us to recheck these structures with respect to the hydrogen atom orientation and energy with the help of further QM calculations.

3.1.5. Scenario THREE: is the hydrogen atom orientation important? The compounds PYD and PD were analyzed carefully

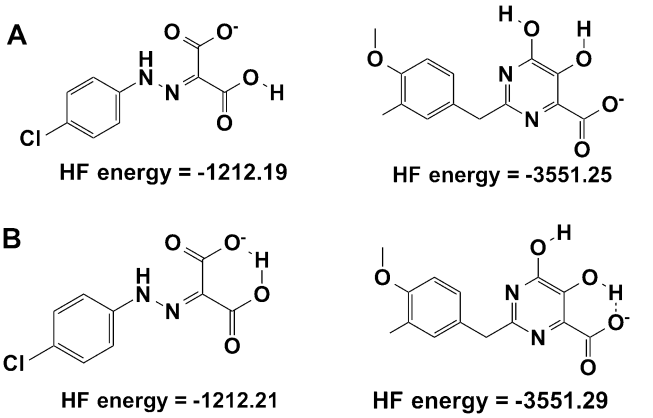

Fig. 4 Comparison of total energies in a.u. calculated with and without the intra-molecular hydrogen bonding network in the initial structure for molecular dynamics simulations.

including the orientation of the hydrogen atoms of the hydroxyl groups close to the deprotonated carboxylic acid and carboxylic acid group, respectively. This proton could be shared inter-molecularly between two oxygen atoms because of intra-molecular hydrogen bonding. We noticed that the hydrogen atom attached to the hydroxyl oxygen (*i.e.* C(O$^-$)–OH) atom neighboring the deprotonated carboxylic acid is positioned as pointing towards oxygen atoms in both compounds. In order to further confirm that this form shown in Fig. 4B is the most preferable one, we performed additional energy optimization calculation (HF/6-31G**) using Gaussian 09. As expected, the structures shown in Fig. 4B possess lower energies compared to the structures shown in Fig. 4A. Therefore an additional MD simulation was performed for PD and PYD according to the 4B forms shown in Fig. 4B.

3.1.6. Scenario THREE: results. The obtained binding free energies for compounds PD and PYD are provided in Table 1 (scenario THREE) and the correlation between the calculated and experimental activities is shown in Fig. 3C. It is clear from the correlation coefficient of MM-GB/SA (R^2 = 0.83) and MM-PB/SA (R^2 = 0.61) that indeed the intra-molecular hydrogen bonds play a significant role in the overall binding free energy of the compounds PYD and PD, as both compounds are now closer to

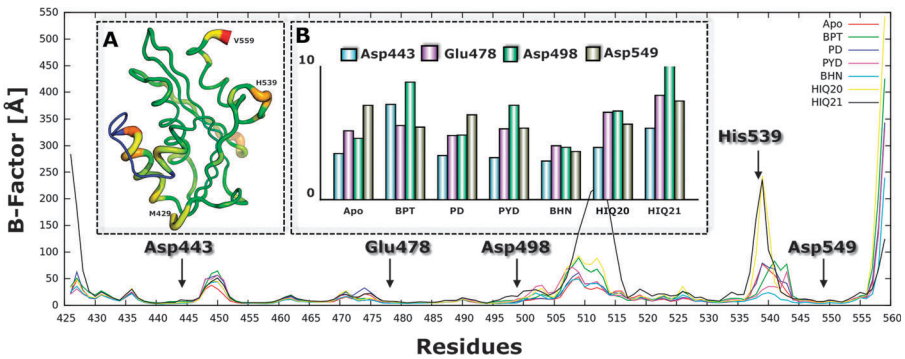

Fig. 5 Average root-mean square fluctuation of protein backbone atoms as a function of residue number for all complexes, including ligand free simulation. Panel A shows the *R*-factor according to the X-ray crystal structure and panel B shows RMSF of conserved residues for all complexes.

the trend line. Furthermore, it is noteworthy that the ranking of the observed activity is consistent with our free energy based predictions.

From the part 1 results, it is summarized that in both the MM-PB/SA and MM-GB/SA methods, the van der Waals term for all the compounds is unfavorable and has the least contribution to the binding energy, whereas the electrostatic term is favorable and dominates the overall binding affinity for all the compounds. In general with respect to correct ranking according to the experimental activities, the MM-GB/SA (r^2 = 0.84) method performs better than MM-PB/SA (r^2 = 0.61). Having seen now the importance of using the correct ligand protonation states in the docking, MD and free energy calculations we will now investigate in more detail the structural dynamics of RNH in both ligand-free and complex forms. The analysis will be performed for the settings described in scenario THREE.

3.2. Part 2: structural dynamics of RNase H

To assess the stability of all considered complexes, the atom-positional root-mean-square deviation (RMSD) of the backbone atoms (αC, N, C) of the protein relative to the initial structure was analyzed for the 2000 snapshots extracted from the 20 ns

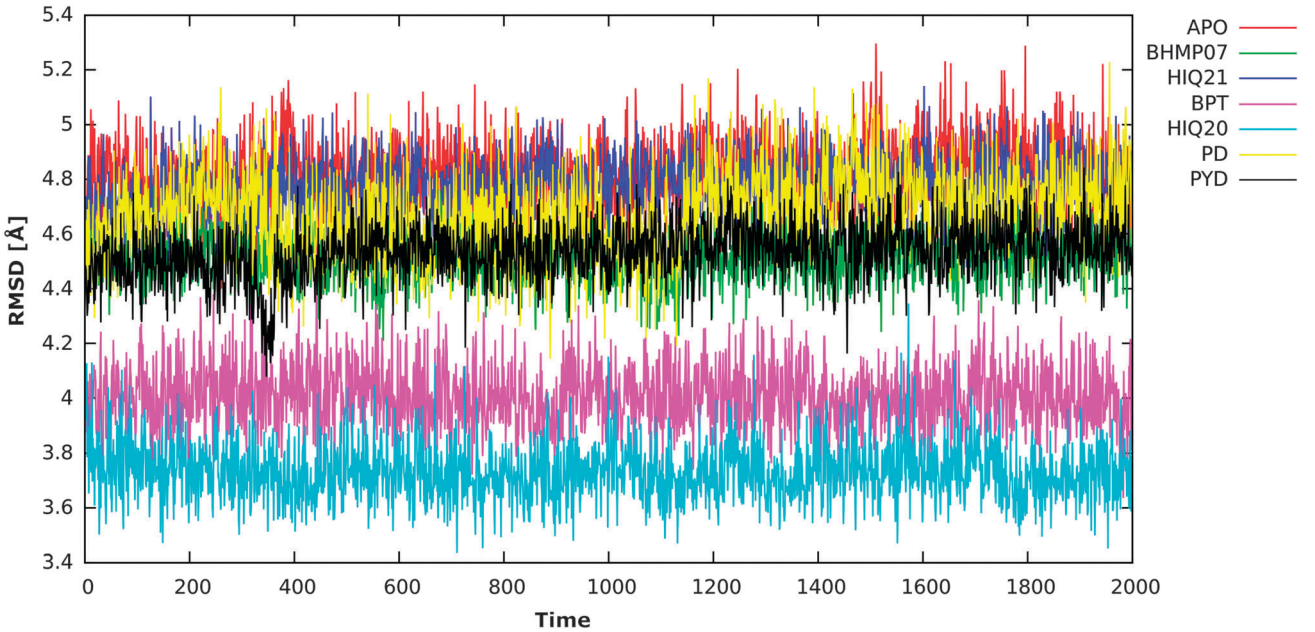

Fig. 6 Distance between two catalytically active magnesium ions as a function of time for all complex and ligand free simulations.

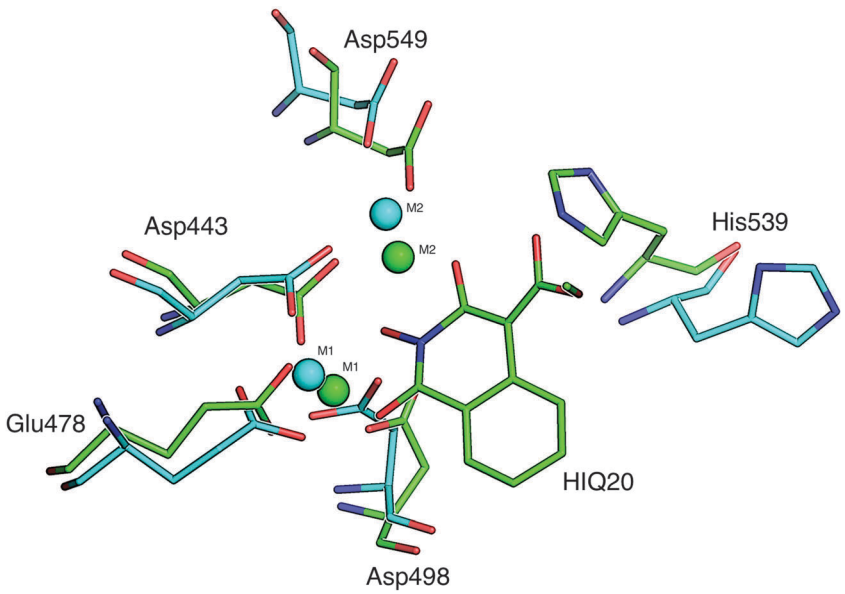

Fig. 7 Superposition of the active site residue conformations of ligand free simulation (cyan) and HIQ20 complex (green) with RNH is shown (see text for more details).

MD simulation (Fig. S2, ESI†). For all compounds the RMSD for the backbone remains below 1.2 Å after 10 ns simulation compared to the initial structure (Fig. S3, ESI†).

To further evaluate which part of the protein that shows high mobility, the rmsf (*b*-factor) of the backbone atoms (αC, N, C) for each residue was calculated (Fig. 5). It can be seen that residues between 445–455, 505–515 and 535–545 are highly flexible and that this fluctuation is also slightly different for different complexes. For instance, residues between 505–515 and 535–545 when complexed with HIQ21 and HIQ20 are highly fluctuating compared to the other complexes. The residues show relatively low flexibility for the RNH–BHMP07 complex. Overall, the order of flexibility is increasing as follows: BHMP07 (9) < PYD (6) < PD (5) < BPT (3) < HIQ20 (2) < HIQ21 (1) and this correlates perfectly with the number of rotatable bonds of the ligands (shown in the brackets). The flexibility of the conserved residues (Asp443, Glu478, Asp498 and Asp549) is found to be quite low throughout the simulations for all the complexes. His539 shows high flexibility for all complexes and, as seen in our previous study,[18] His539 plays a significant role in the formation of π or π–cation interactions during the accommodation of ligands in the binding cavity.

3.2.1. Magnesium ions dynamics. The dynamics of the two magnesium ions were analyzed for both the free and ligand-bound RNH. As seen from Fig. 6, the magnesium ions are dynamic and move either away or close to each other throughout the simulations. Interestingly, except for the highly active compound HIQ20, the inter-magnesium ion distance is greatly increased throughout the simulations. For instance, the distance between the magnesium ions in the ligand free simulation (*i.e.*, Apo form) of RNH is found to be highest in all case (~4.9 Å), followed by the least active compound HIQ21 where the magnesium distance is ~4.8 Å. Here, the distance is also highly correlated with the RNH inhibition potency of the ligands, where a higher inhibition potency correlates with a lower distance between the magnesium ions. Compared to the magnesium ion distance from the X-ray crystal structure (3.8 Å), the observed distance in the Apo form is very large (4.9 Å). This indicates that when the negatively charged reactive group of the ligands approaches the active site, the magnesium ions move

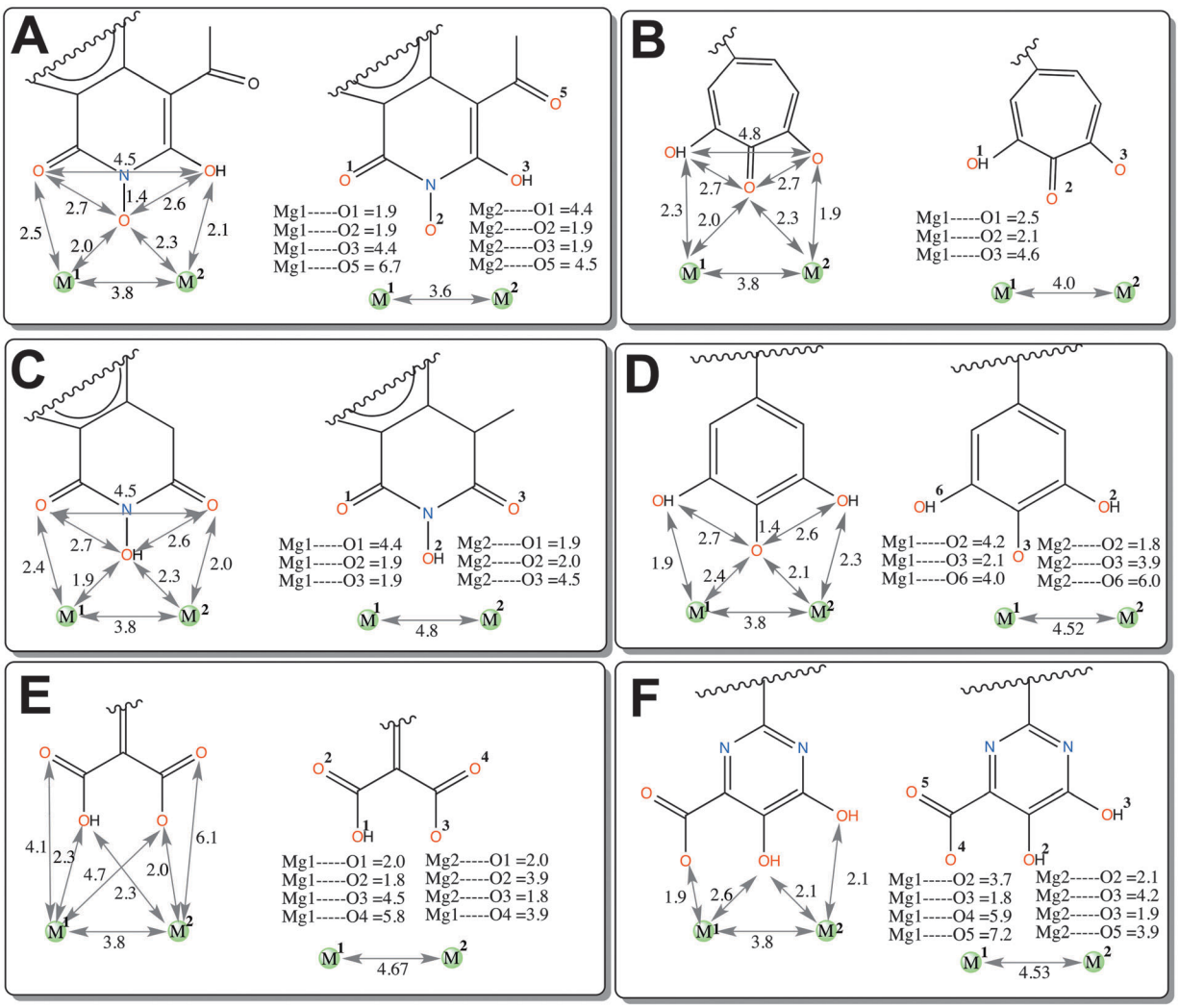

Fig. 8 Average interatomic distance between Mg^{2+} and ligands as a function of time. Panel A: HIQ20, B: BPT, C: HIQ21, D: BHMP07, E: PD and F: PYD.

closer to each other in order to make a strong ligand–magnesium ion chelation complex, which impacts the overall inhibition potency of the compounds as observed previously.[37] A snapshot comparing the magnesium ion positions in the Apo form and in the HIQ20 complex from the simulation is shown in Fig. 7. Particularly, His539 is pointing towards the ligand in

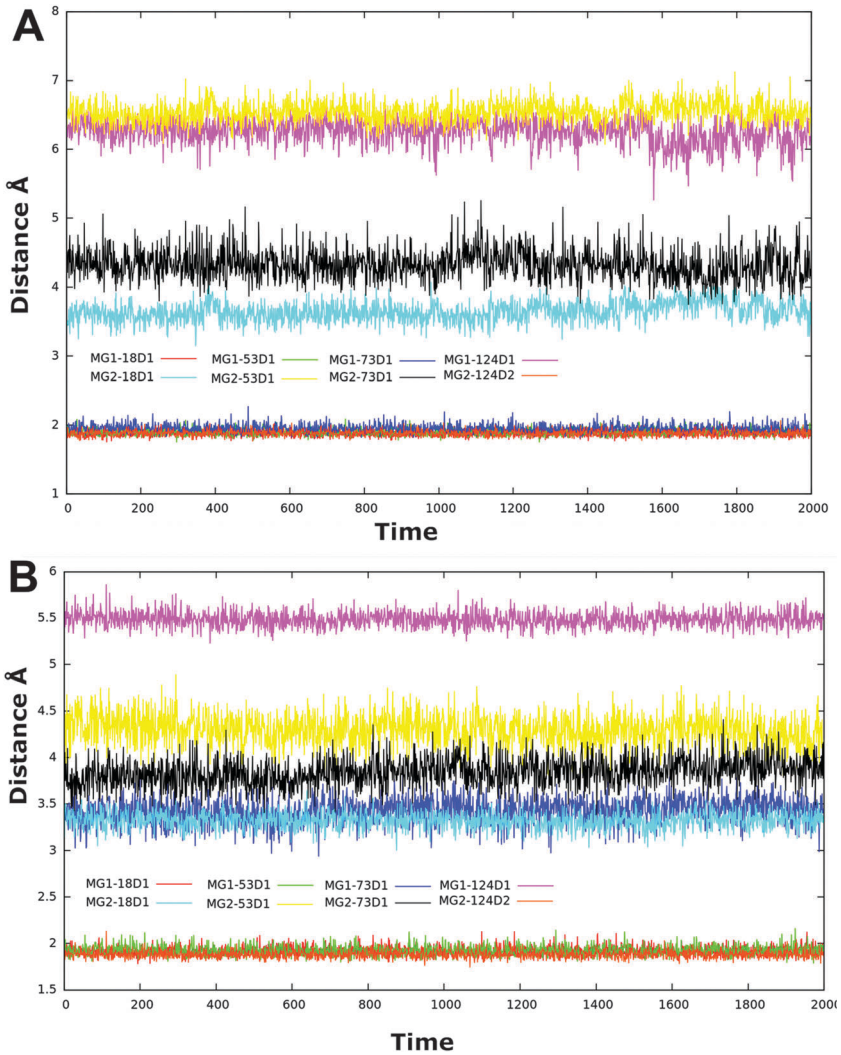

Fig. 9 Time series of magnesium ions–residues distance of ligand free simulation of RNase H (A), RNase H–HIQ20 complex (B).

Fig. 10 Snapshots of the active site of the RNH–HIQ20 complex; (A) active site in the starting structure; (B) active site shown after 100 ps simulation, (C) active site shown after 10 ns simulation. Important residues and HIQ20 are highlighted with the ball and stick model. Magnesium ions are shown in orange sphere and various water molecules are shown using red, green and cyan spheres.

order to make favorable hydrogen bonding or π or π–cation interactions.

3.2.2. Magnesium ion–ligand interactions. It has been observed from our previous study[37] that the inhibition potency of the ligand is greatly correlated with the strength of the magnesium–ligand chelation energy. Therefore, we now turn our attention to how often the magnesium ions interact with the ligand reactive site oxygen atoms as a function of time. As illustrated in Fig. 8, in all complexes, the ligands coordinate favorably with the two magnesium ions in the active site throughout the simulation. For instance, HIQ20 (high potency compound) and HIQ21 (low potency compound) share the same scaffold as well as number of oxygen atoms at the reactive site, however, these compounds possess different protonation states which leads to differences in the strength of the chelation energy. In general, although the "pharmacophoric" pattern of these compounds is very similar, different ligands give rise to varying distances between the ligand oxygen atoms and magnesium ions. For instance, the distance between the oxygen atoms of HIQ20 (O2) with Mg1 and Mg2 remains ~2.0 Å throughout the simulation compared to the distance observed between the O1 and O3 atoms with Mg1 and Mg2. An additional carbonyl oxygen atom (O5) interacts weakly with Mg2 with a distance of 4.4 Å which is slightly smaller than the distance observed in the initial structure (5.5 Å). Although this distance is quite large for chelation, this would still give an additive effect to chelation of O1, O2 with Mg1 and O2, O3 with Mg2 coordination for chelation (see Fig. 8). It should be noted that both HIQ20 and HIQ21 show a similar "Mg–O" overall distance pattern, however, for compound HIQ21, the inter-metal distance is quite large and only one oxygen atom binds to the magnesium ions which all significantly reduces the strength of overall chelation.

Compared to the other compounds in the dataset, compounds PD and PYD are relatively acidic in nature, as these both possess carboxylic acid groups. The overall charge of both compounds is −1. Although, the oxygen atoms of both compounds are very close to the magnesium ions, only O3 of compound PD and O4 of compound PYD interact favorably with magnesium ions due to the unfavorable charge–charge interaction of the other oxygen atoms which reduce the overall strength of the chelation and this causes a reduced ligand affinity compared to HIQ20 as discussed in Section 2.1.5.

3.2.3. Magnesium ion–residues interactions. A magnesium ion residue interaction analysis was performed using the 2000 snapshots for all complexes and ligand free simulations with the aim to compare the difference in the Mg–residue coordination especially between the conserved residues. It can be seen from the ligand free RNH simulation (Fig. 9A) that there is no significant fluctuation found throughout the simulation, meaning that the distance of the magnesium ions and the corresponding residues (Asp443, Glu478, Asp498 and Asp549) is maintained throughout the simulation. The distances between Mg1 and the oxygen atoms of Asp443, Glu478, Asp498 are ~2 Å and the distances between Mg2 and the residues are quite large (>4 Å).

A comparison of the distances between the magnesium ions and residues for the Apo and complex simulations may provide valuable information about the active site dynamics upon ligand binding. Thus, the distance between the oxygen atoms of the conserved residues and Mg^{2+} is compared based on the Apo and complex simulations. As seen from Fig. 9B, the distance between the

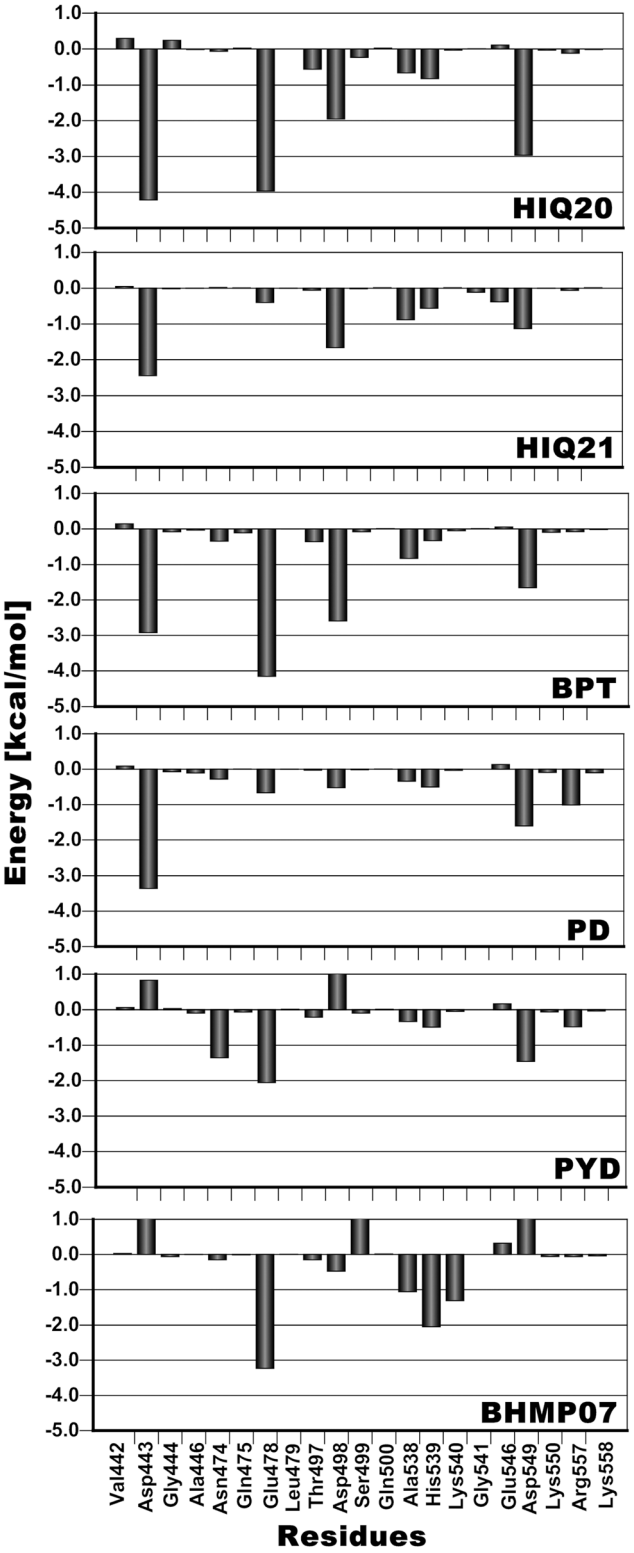

Fig. 11 Residue decomposition of the binding free energies.

magnesium–residue coordination is significantly decreased in the RNH–HIQ20 complex compared to the Apo form. For instance, Mg1–Asp549 (6.3 → 5.5), Mg2–Asp443 (3.8 → 3.4), Mg2–Glu478 (6.5 → 4.5) and Mg2–Asp498 (4.5 → 3.8) in HIQ20 compared to the ligand-free form. Similar results were observed for other ligand complexes as well. This observation indicates that the ligand-free enzyme possesses a relatively large cavity and upon ligand binding the cavity shrinks in order to provide a best fit for the ligand binding.

3.2.4. Active site water dynamics. It is well known from the reported crystal structure of HIV-1 RNase H with a bound inhibitor (*N*-hydroxy quinazolidione) that two water molecules at the active site are tightly coordinated with metal A (*i.e.* Mg1). These water molecules act as the nucleophiles upon metal mediated activation. It has previously been observed in docking based virtual screening that the role of the water molecules at the active site is essential for inhibitor binding, for instance, bound waters no. 17 and 24 are found to form hydrogen bonding with 40% of the inhibitors used in the dataset.[37] In this study, water molecules that are located within 3 Å from the ligand were included (water no. 15, 17, 24, 118, 156, 562 and 563). The role of water molecules for RNH function and inhibitor binding is uncertain, therefore a detailed study of water mediated hydrogen bonding was performed. From a hydrogen bond analysis a number of hydrogen bonds between the magnesium ions and water molecules in the active site are found in all simulations (Fig. 10). It was observed that some water molecules at the active site are very dynamic and some are stable throughout the simulation. For instance, the water molecules no. 15, 17, 118 and 156 instantly move from their original position and did not perform hydrogen bonding either with ligands or magnesium ions throughout the simulation. After 100 ps water molecule no. 24 did not perform contacts with any of the interaction partners such as protein or ligands in the rest of the simulation (Fig. 10B). Conversely, water molecule no. 562 and 563 were tightly coordinated to the magnesium ion (1) throughout the simulation and these water molecules did not move or exchange with the bulk waters. The average distance between Mg1 with water no. 562 and water no. 563 were found to be 2.015 and 2.010 Å, respectively (Fig. 10C). The magnesium ion (2) did not perform hydrogen bonding with any of these bound water molecules. This finding is in good agreement with the observed contacts in the recent crystal structure.[15] None of the crystal structure water molecules participate in hydrogen bonding networks with inhibitors except water no. 24 which possesses a very short contact with the inhibitors. This shows that water molecules at the RNH active site do not directly influence the inhibitor binding, but water no. 562 and 563 are very crucial in order to stabilize the magnesium ion (preferably, Mg1) coordination with conserved residues such as Asp549 and Asp443. Although the hydrogen bonding interaction is included in the electrostatic interaction term of the binding free energy calculations, the binding affinity of these compounds is mainly driven by the chelation energy between magnesium ions and inhibitors; this has recently been validated using QM based chelation calculations.[37]

3.2.5. Decomposition analysis of the binding free energies. The aim of this energy decomposition analysis is to examine the role of individual residue contributions to the overall binding affinity of the compounds by decomposition of the binding free energy into inhibitor–residue pairs. The energy contributions between each residue of RNH and inhibitors are plotted in Fig. 11. As seen from the decomposition analysis plot, all six inhibitors show relatively different interactions with the RNH residues during the simulation. For instance, residues Glu478, Ala538, His539 and Arg557 all show a favorable energy contribution to the binding affinity of all compounds, and negatively charged residues such as Asp443, Asp498, Asp549 also show a high favorable energy contribution for most of the compounds, except the inhibitors PYD and BHMP07. These two compounds possess unfavorable interactions with residue Asp443 ($\sim$1 kcal mol^{-1}). Furthermore, the residues Asp498 and Asp549 yield an unfavorable energy contribution to PYD and BHMP07 compounds, respectively. The inhibitor affinity to the protein is highly correlated with binding energy contributions from residues Glu478 and Thr497 (Table 2). The correlation (R^2) between the binding affinity and energy contributions due to Glu478 and Thr497 is found to be 0.91 and 0.68 respectively (Fig. S4, ESI†). We also correlated the observed activity with binding energy contributions of only the magnesium ions. This leads to a relatively good model (R^2 = 0.73) and furthermore this correlation improves to R^2 = 0.78 upon adding Glu478 and Thr497 energy contributions. Overall, this observation strongly suggests that the chelation mechanism is one of the main driving forces that control the overall ligand binding as observed previously.[37]

Table 2 Summary of decomposition analysis of the binding free energies obtained from the MM-GB/SA method

Compounds	pIC_{50}	ΔG*	Thr497, Glu478 (−)	Mg, Thr497, Glu478 (−)	Mg (−)	Mg, ligand (+)	Thr497, Glu478 (+)	Ligand (+)	Ligand, Thr498, Glu478 (+)	Mg, Ligand, Thr498, Glu478 (+)
HIQ20	7.21	−48.46	−43.67	−10.23	−14.76	−33.44	−4.53	−66.43	−70.96	−37.976
HIQ21	4.41	−3.20	−2.74	−7.94	−8.40	5.2	−0.46	−13.79	−14.25	4.748
BPT	6.68	−37.51	−32.99	−7.66	−12.18	−25.32	−4.52	−49.13	−53.65	−29.849
PD	5.21	−10.85	−10.17	−8.24	−8.93	−1.92	−0.68	−33.09	−33.77	−2.616
PYD	6.05	−42.79	−40.53	−1.81	−4.08	−38.71	−2.26	−40.47	−42.73	−40.98
BHNP07	6.7	−30.77	−27.38	0.35	−3.03	−27.74	−3.38	−28.93	−32.32	−31.124
R^2		0.82	0.79	0.02	0.05	0.73	0.91	0.67	0.71	0.78

The results refer to averages over 2000 frames and all units are reported in kcal mol^{-1}. * According to the MM-GBSA model, extracted from the differences (average) of $\Delta G_{Complex} - \Delta G_{Receptor} - \Delta G_{Ligand}$. + Indicates only the energy of these components are used for correlation with observed activities. − Indicates other than these components are used for correlation with observed activities.

4. Conclusion

In the present study MM-PB(GB)/SA methods have been used as an initial validation for a structural dynamic analysis of RNH–inhibitor complexes using molecular dynamics simulations. From the MM-PB(GB)/SA study it is found that the electrostatic interactions dominate the overall binding affinities compared to the van der Waals (vdW) energy contribution. In terms of the ability to correctly rank the ligands according to experimental activities the MM-GBSA (R^2 = 0.84) method performs better than MM-PBSA (R^2 = 0.61). This study has especially been performed in order to unveil the overall structural dynamics of RNH and this analysis includes both ligand-free and complex simulations. From the snapshots extracted from a 20 ns simulation, inter-atomic distance analysis of the two magnesium ions reveals that the magnesium ions are very dynamic and that the distance is significantly changed for different ligands compared to the original distance (3.8 Å). The minimum distance (3.6 Å) was found for a highly active compound (HIQ20) and a maximum distance (4.67 Å) was found for a low active compound (PD). In addition to the inter-atomic distance between the magnesium ions, the protonation states of the ligands also play a crucial role in how well they bind with magnesium ions. For instance, HIQ20 (IC_{50} = 0.061 μM) and HIQ21 (IC_{50} = 38.8 μM) both possess very similar structural features, however, they have different protonation states, which results in HIQ20 being a highly active compound. In all cases residues Glu478 and Thr497 show very favorable interaction with the ligands. In addition, residues such as Ala445, Asn474, Ala538, His539 and Arg555 also showed favorable energy contributions to the overall ligand binding either by hydrogen bonding or π interactions. From the water dynamics analysis it is found that at least two water molecules at the active site coordinate with the magnesium ions throughout the simulation. Overall, the RNH structure is very stable, however, it slightly decreases the active site volume when the ligands bind. The analysis provided in this study could provide valuable information for the RNH inhibitor design.

Acknowledgements

The authors are thankful for financial support from the Lundbeck Foundation, The Danish Councils for Independent Research, the Villum Foundation, Denmark. The authors are also thankful to ChemAxon and OpenEye scientific software for providing a free academic license.

References

1 E. De Clercq, *Biochim. Biophys. Acta, Mol. Basis Dis.*, 2002, **1587**, 258–275.
2 A. S. Fauci, *Nat. Med.*, 2003, **9**, 839–843.
3 D. M. Himmel, K. A. Maegley, T. A. Pauly, J. D. Bauman, K. Das, C. Dharia, A. D. Clark Jr., K. Ryan, M. J. Hickey, R. A. Love, S. H. Hughes, S. Bergqvist and E. Arnold, *Structure*, 2009, **17**, 1625–1635.
4 A. J. Ribeiro, M. J. Ramos and P. A. Fernandes, *J. Am. Chem. Soc.*, 2012, **134**, 13436–13447.
5 P. Bean, *Clin. Infect. Dis.*, 2005, **41**(suppl 1), S96–S100.
6 FDA, Antiretroviral drugs used in the treatment of HIV infection, http://www.fda.gov.
7 E. Tramontano and R. Di Santo, *Curr. Med. Chem.*, 2010, **17**, 2837–2853.
8 T. Ilina, K. Labarge, S. G. Sarafianos, R. Ishima and M. A. Parniak, *Biology*, 2012, **1**, 521–541.
9 D. M. Himmel, S. G. Sarafianos, S. Dharmasena, M. M. Hossain, K. McCoy-Simandle, T. Ilina, A. D. Clark Jr., J. L. Knight, J. G. Julias, P. K. Clark, K. Krogh-Jespersen, R. M. Levy, S. H. Hughes, M. A. Parniak and E. Arnold, *ACS Chem. Biol.*, 2006, **1**, 702–712.
10 M. Wendeler, H. F. Lee, A. Bermingham, J. T. Miller, O. Chertov, M. K. Bona, N. S. Baichoo, M. Ehteshami, J. Beutler, B. R. O'Keefe, M. Gotte, M. Kvaratskhelia and S. Le Grice, *ACS Chem. Biol.*, 2008, **3**, 635–644.
11 A. K. Felts, K. Labarge, J. D. Bauman, D. V. Patel, D. M. Himmel, E. Arnold, M. A. Parniak and R. M. Levy, *J. Chem. Inf. Model.*, 2011, **51**, 1986–1998.
12 M. Nowotny, S. A. Gaidamakov, R. Ghirlando, S. M. Cerritelli, R. J. Crouch and W. Yang, *Mol. Cell*, 2007, **28**, 264–276.
13 R. Costi, M. Métifiot, F. Esposito, G. Cuzzucoli Crucitti, L. Pescatori, A. Messore, L. Scipione, S. Tortorella, L. Zinzula, E. Novellino, Y. Pommier, E. Tramontano, C. Marchand and R. Di Santo, *J. Med. Chem.*, 2013, **56**, 8588–8598.
14 J. D. Barlett, Medscaps, 2006, Feb. 8, http://www.medscape.org/viewarticle/523119.
15 E. B. Lansdon, Q. Liu, S. A. Leavitt, M. Balakrishnan, J. K. Perry, C. Lancaster-Moyer, N. Kutty, X. Liu, N. H. Squires, W. J. Watkins and T. A. Kirschberg, *Antimicrob. Agents Chemother.*, 2011, **55**, 2905–2915.
16 H. P. Su, Y. Yan, G. S. Prasad, R. F. Smith, C. L. Daniels, P. D. Abeywickrema, J. C. Reid, H. M. Loughran, M. Kornienko, S. Sharma, J. A. Grobler, B. Xu, V. Sardana, T. J. Allison, P. D. Williams, P. L. Darke, D. J. Hazuda and S. Munshi, *J. Virol.*, 2010, **84**, 7625–7633.
17 M. Billamboz, F. Bailly, C. Lion, N. Touati, H. Vezin, C. Calmels, M. L. Andreola, F. Christ, Z. Debyser and P. Cotelle, *J. Med. Chem.*, 2011, **54**, 1812–1824.
18 P. Vasanthanathan and J. Kongsted, *PLoS One*, 2013, **8**, e73478, 1–15.
19 H. Fuji, E. Urano, Y. Futahashi, M. Hamatake, J. Tatsumi, T. Hoshino, Y. Morikawa, N. Yamamoto and J. Komano, *J. Med. Chem.*, 2009, **52**, 1380–1387.
20 S. Distinto, F. Esposito, J. Kirchmair, M. C. Cardia, M. Gaspari, E. Maccioni, S. Alcaro, P. Markt, G. Wolber, L. Zinzula and E. Tramontano, *Eur. J. Med. Chem.*, 2012, **50**, 216–229.
21 H. Yanagita, S. Fudo, E. Urano, R. Ichikawa, M. Ogata, M. Yokota, T. Murakami, H. Wu, J. Chiba, J. Komano and T. Hoshino, *Chem. Pharm. Bull.*, 2012, **60**, 764–771.
22 K. Arnold, L. Bordoli, J. Kopp and T. Schwede, *Bioinformatics*, 2006, **22**, 195–201.
23 Schrödinger, Portland, USA, 2013.

24 G. Madhavi Sastry, M. Adzhigirey, T. Day, R. Annabhimoju and W. Sherman, *J. Comput.-Aided Mol. Des.*, 2013, **27**, 221–234.
25 H. Li, A. D. Robertson and J. H. Jensen, *Proteins*, 2005, **61**, 704–721.
26 M. T. Christen, L. Menon, N. S. Myshakina, J. Ahn, M. A. Parniak and R. Ishima, *Chem. Biol. Drug Des.*, 2012, **80**, 706–716.
27 J. C. Shelley, A. Cholleti, L. L. Frye, J. R. Greenwood, M. R. Timlin and M. Uchimaya, *J. Comput.-Aided Mol. Des.*, 2007, **21**, 681–691.
28 A. D. Bochevarov, E. Harder, T. F. Hughes, J. R. Greenwood, D. A. Braden, D. M. Philipp, D. Rinaldo, M. D. Halls, J. Zhang and R. A. Friesner, *Int. J. Quantum Chem.*, 2013, **113**, 2110–2142.
29 R. A. Friesner, J. L. Banks, R. B. Murphy, T. A. Halgren, J. J. Klicic, D. T. Mainz, M. P. Repasky, E. H. Knoll, M. Shelley, J. K. Perry, D. E. Shaw, P. Francis and P. S. Shenkin, *J. Med. Chem.*, 2004, **47**, 1739–1749.
30 D. A. Case, T. A. Darden, I. T. E. Cheatham, C. L. Simmerling, J. Wang, R. E. Duke, R. Luo, R. C. Walker, W. Zhang, K. M. Merz, B. Roberts, S. Hayik, A. Roitberg, G. Seabra, J. Swails, A. W. Goetz, I. Kolossváry, K. F. Wong, F. Paesani, J. Vanicek, R. M. Wolf, J. Liu, X. Wu, S. R. Brozell, T. Steinbrecher, H. Gohlke, Q. Cai, X. Ye, J. Wang, M.-J. Hsieh, G. Cui, D. R. Roe, D. H. Mathews, M. G. Seetin, R. Salomon-Ferrer, C. Sagui, V. Babin, T. Luchko, S. Gusarov, A. Kovalenko and P. A. Kollman, *Amber 12*, University of California, San Francisco, 12 edn, 2012.
31 M. J. Frisch, G. W. Trucks, H. B. Schlegel, G. E. Scuseria, M. A. Robb, J. R. Cheeseman, G. Scalmani, V. Barone, B. Mennucci, G. A. Petersson, H. Nakatsuji, M. Caricato, X. Li, H. P. Hratchian, A. F. Izmaylov, J. Bloino, G. Zheng, J. L. Sonnenberg, M. Hada, M. Ehara, K. Toyota, R. Fukuda, J. Hasegawa, M. Ishida, T. Nakajima, Y. Honda, O. Kitao, H. Nakai, T. Vreven, J. A. Montgomery Jr., J. E. Peralta, F. Ogliaro, M. Bearpark, J. J. Heyd, E. Brothers, K. N. Kudin, V. N. Staroverov, R. Kobayashi, J. Normand, K. Raghavachari, A. Rendell, J. C. Burant, S. S. Iyengar, J. Tomasi, M. Cossi, N. Rega, N. J. Millam, M. Klene, J. E. Knox, J. B. Cross, V. Bakken, C. Adamo, J. Jaramillo, R. Gomperts, R. E. Stratmann, O. Yazyev, A. J. Austin, R. Cammi, C. Pomelli, J. W. Ochterski, R. L. Martin, K. Morokuma, V. G. Zakrzewski, G. A. Voth, P. Salvador, J. J. Dannenberg, S. Dapprich, A. D. Daniels, Ö. Farkas, J. B. Foresman, J. V. Ortiz, J. Cioslowski and D. J. Fox, *Gaussian 09*, Gaussian, Inc., Wallingford, CT, USA, Revision D.01 edn., 2009.
32 H. J. C. Berendsen, J. P. M. Postma, W. F. van Gunsteren, A. DiNola and J. R. Haak, *J. Chem. Phys.*, 1984, **81**, 3684–3690.
33 J. M. Hayes and G. Archontis, in *Molecular Dynamics – Studies of Synthetic and Biological Macromolecules*, ed. L. Wang, InTeck, 2012, ch. 9.
34 A. Weis, K. Katebzadeh, P. Soderhjelm, I. Nilsson and U. Ryde, *J. Med. Chem.*, 2006, **49**, 6596–6606.
35 J. Kongsted and U. Ryde, *J. Comput.-Aided Mol. Des.*, 2009, **23**, 63–71.
36 B. R. Miller, T. D. McGee, J. M. Swails, N. Homeyer, H. Gohlke and A. E. Roitberg, *J. Chem. Theory Comput.*, 2012, **8**, 3314–3321.
37 V. Poongavanam, C. Steinmann and J. Kongsted, *PLoS One*, 2014, **9**, e98659, 1–11.